IOP Publishing Journal of Physics: Condensed Matter
J. Phys.: Condens. Matter **32** (2020) 285302 (8pp) https://doi.org/10.1088/1361-648X/ab8154

Thermal magnetoresistance and spin thermopower in C_{60} dimers

Majid Shirdel-Havar and Rouhollah Farghadan

Department of Physics, University of Kashan, Kashan, 87317-53153, Iran

E-mail: rfarghadan@kashanu.ac.ir

Received 19 September 2019, revised 11 March 2020
Accepted for publication 19 March 2020
Published 17 April 2020

Abstract

We theoretically investigate the spin-related thermoelectric properties in C_{60} dimer bridged between zigzag graphene nanoribbon electrodes using the tight-binding model, equilibrium Green's function method, and Landauer–Büttiker transport formalism. By applying a thermal gradient, our proposed device could generate a notable spin thermopower. Moreover, by switching the magnetization of the electrodes, different spin currents, and giant thermal magnetoresistance (MR) can be achieved. Interestingly, various types of C_{60} dimers also produce a thermal MR, which is sensitively modified by the gate voltages.

Keywords: thermal magnetoresistance, spin thermopower, C60 dimers, zigzag graphene nanoribbon

(Some figures may appear in colour only in the online journal)

1. Introduction

For over two decades, organic molecular materials (OMMs) have emerged as one of the attractive candidates for molecular spintronic devices (MSDs). This attention is mainly due to the capability of manipulating spin polarization of electrons in the molecular junctions [1, 2]. Also, the low spin–orbit coupling and weak hyperfine interaction in OMMs produce the long spin-relaxation time and spin-diffusion length [3, 4]. Fullerene C_{60} because of the ability to maintain the spin polarization of carriers on time scales of milliseconds [5, 6] and large spin transport on length scales about a few hundred nanometers at room temperature [7, 8] can be a promising candidate for organic MSDs.

In recent years, the injection and controlling of the spin current through the fullerene C_{60} sandwiched between two magnetic or nonmagnetic electrodes have been investigated, experimentally [8–14] and theoretically [15, 16]. In detail, C_{60}-devices produce a magnetoresistance (MR) effect, when the magnetization of the electrodes switches from the parallel to antiparallel configuration and vice versa. An important challenge in spin-dependent transport in these devices is the ability to inject spins from a ferromagnetic (FM) electrode into an organic molecular. The spin injection process in MSDs is heavily influenced by the interface between organic molecules and spin-resolved electronic states of the FM electrode [17, 18]. A close match between FM electrode's Fermi energy and organic molecule's HOMO and LUMO can facilitate the spin injection process. In this regard, carbon-based material can be a promising candidate as an electrode in organic MSDs [19]. Therefore spin injection process can be guaranteed in all-carbon junction.

C_{60} anchor groups have been used as a molecular bridge between graphene nanoelectrodes in single-molecule electronics in recent experiments [20, 21]. The results propose that C_{60}/graphene combination can be used for practical applications in single-molecule energy-conversion devices. Furthermore, C_{60}-based molecular junctions with metallic electrodes (i.e., Pt, Au, Ag, Ni) have been proposed to exploit thermoelectric (TE) effects of OMMs [22–27]. Recently, C_{60}/graphene combination have been designed as vertical graphene–C_{60}–graphene to investigate the TE effects, theoretically [28]. The results indicate TE effects can be improved due to inter-junction quantum interference, mediated by the number of parallel C_{60} molecules sandwiched between the graphene electrodes in this vertical molecular device. Moreover, the TE properties of graphene-fullerene nanodevices were studied experimentally at different temperatures, and the results show that the electric field can control the TE coefficients [29]. Generally, reliable approaches to integrate

individual or a small collection of molecules into molecular-scale nanocircuits has been highly developed based on carbon nanoelectrodes [20, 21]. Also, the possibility of applying gate voltage and temperature gradient across the actual molecular junctions to measure the thermoelectric properties has been confirmed in recent experiments [22]. Moreover, the effects of dopant nitrogen on the TE properties of C_{60} bridged between graphene nanoribbons (GNRs) have been studied [30]. However, the possibility of generating a thermal spin current in C_{60}-based molecular junctions with GNRs have not been investigated.

Here, we consider fullerene C_{60} dimer bridged between zigzag GNRs (ZGNRs) electrodes as a spin TE device and theoretically studied its thermally spin-transport effects in FM and anti-FM (AFM) configurations. The results indicate substantial variations of transmission around the Fermi level in one of the spin channels, and the other channel is almost blocked in the FM configuration. These manners lead to thermal spin transport in one of the spin channels of FM configuration and identical transport on both spin channels of AFM configuration under the temperature gradient. Moreover, the maximum value of spin thermopower (TP) is about 710 μV/K. This device indicates giant thermal MR when the junction switches between AFM and FM configurations. Furthermore, we have expanded our computations for different C_{60} dimers in the presence of gate voltage. The results demonstrated that these structures could be applied in the spin TE devices because of the significant thermal MR effect.

2. Model and method

The C_{60} dimer is produced through the energetically bonding between the two C_{60} molecules by a [2 + 2] photocycloaddition reaction [31]. The designed spin TE device consisting of C_{60} dimer bridged between two 6-ZGNRs for AFM and FM configurations are illustrated in figures 1(a) and (b), respectively. We denote this structure briefly with ZZ-C60D-ZZ. Note that, in FM (AFM) configuration, both electrodes have similar FM (AFM) spin orientation. For example, the magnetization direction of each electrode in the AFM configuration (ground state) is antiparallel. The FM configuration can achieve by applying a magnetic field [32]. Interestingly, zigzag-edges magnetism can be preserved at room temperature [33]. To study spin TE effects, we first computed the electronic transport using the equilibrium Green's function approach and the Landauer–Büttiker transport formalism [34, 35]. Then, we computed the thermospin coefficients using electron transmission functions. To this purpose, the infinite device is divided into three regions, namely, a scattering region, containing the C_{60} dimer, which is connected to the right (R) and left (L) semi-infinite ZGNR electrodes. The Hamiltonian matrix describing the whole device is then given by

$$\mathcal{H} = \mathcal{H}_{\rm C} + \mathcal{H}_{\rm L} + \mathcal{H}_{\rm R} + \mathcal{V}_{\rm CL} + \mathcal{V}_{\rm CR}, \tag{1}$$

where, $\mathcal{H}_{\rm C}$, $\mathcal{H}_{\rm L}$ and $\mathcal{H}_{\rm R}$ are the Hamiltonian matrices of the scattering region, left, and right electrodes, respectively. $\mathcal{H}_{\rm C}$

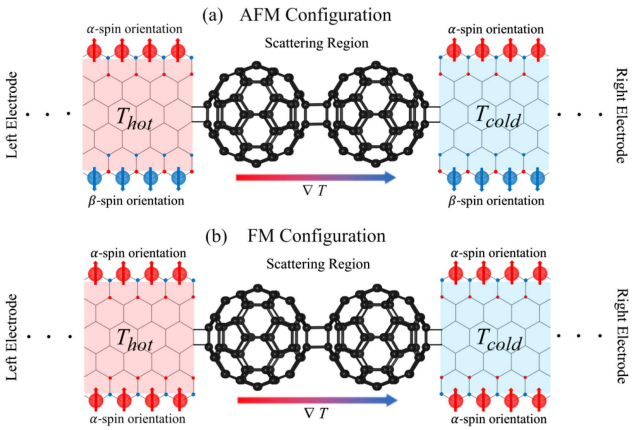

Figure 1. (a) and (b) illustrate the C_{60} dimer which bridged between two 6-ZGNR in AFM and FM configurations, respectively. Red and blue circles represent the α- and β-spin, respectively.

is constructed in the tight-binding (TB) model limited to p_z-orbitals and written as follows

$$\mathcal{H}_{\rm tb} = -\sum_{\langle i,j\rangle,\sigma} t_{i,j} d^{\dagger}_{i\sigma} d_{j\sigma}, \tag{2}$$

$\mathcal{H}_{\rm tb}$ is a noninteracting (without e–e interaction) Hamiltonian, where $t_{i,j}$ is the nearest-neighbor hopping between p_z-orbitals and $d^{\dagger}_{i,\sigma}$ ($d_{j,\sigma}$) is creation (annihilation) operator in the site $i(j)$ with the spin $\sigma(\alpha, \beta)$. In detail, the eigenvalues of the noninteracting Hamiltonian of the C_{60} molecule do not change in the presence of e–e interaction, indicating that this interaction does not have a significant effect on the electronic energy levels of C_{60}. $\mathcal{H}_{\rm C}$ is a 120 × 120 matrix, regarding to 120 atomic sites in the scattering region. We considered different values for $t_{i,j}$ corresponding to C–C single and double bonds length of C_{60} dimer. $t' \simeq 2.5$ eV for single and $t'' \simeq 2.72$ eV for double bonds were considered, according to $t''/t' \simeq (r_1/r_2)^2$, $r_1 = 1.46$ Å and $r_2 = 1.4$ Å are single and double bonds length of C_{60}, respectively [36].

In equation (1), $\mathcal{V}_{\rm CL(CR)}$ represent the hopping matrix between the scattering region and the left (right) electrode which is formed based on TB model. In detail, $\mathcal{V}_{\rm CL(CR)}$ is a 120 × 12 matrix, regarding to 12 atomic sites in a unit cell of the left (right) electrode and 120 sites in the scattering region. There is hopping only between two sites of the left (right) electrode and the scattering region at their junction, therefore, only two matrix elements of $\mathcal{V}_{\rm CL(CR)}$ are nonzero. Here, we set $t \simeq 2.6$ eV for hopping in $\mathcal{V}_{\rm CL(CR)}$ matrix.

Furthermore, $\mathcal{H}_{\rm L}$ and $\mathcal{H}_{\rm R}$ are constructed in the TB model in the presence of e–e interaction which in the mean-field Hubbard approximation. Thus, the spin-dependent $\mathcal{H}_{\rm L(R)}$ for a unit cell of the left (right) electrode can be written as the following matrix form

$$\mathcal{H}^{00}_{\rm L(R)} = \begin{pmatrix} \mathcal{H}^{00}_{\rm L(R),\alpha} & 0 \\ 0 & \mathcal{H}^{00}_{\rm L(R),\beta} \end{pmatrix}, \tag{3}$$

where, $\mathcal{H}^{00}_{\rm L(R),\alpha} = \mathcal{H}_{U,\alpha} + \mathcal{H}^{00}_{\rm tb}$ and $\mathcal{H}^{00}_{\rm L(R),\beta} = \mathcal{H}^{00}_{\rm tb} + \mathcal{H}_{U,\beta}$. $\mathcal{H}^{00}_{\rm tb}$ is a 12 × 12 matrix formed on the TB model with the nearest-neighbor hopping $t \simeq 2.6$ eV for a unit cell in the

left (right) electrode. Moreover, $\mathcal{H}_{U,\alpha(\beta)}$ is a 12×12 diagonal matrix with elements calculated based on mean-field Hubbard, as $U\langle n_{i\beta}\rangle[n_{i\alpha} - (1/2)\langle n_{i\alpha}\rangle]$ for α-spin and $U\langle n_{i\alpha}\rangle[n_{i\beta} - (1/2)\langle n_{i\beta}\rangle]$ for β-spin at the site i [37, 38]. $U = 1.06\,t$ is the on-site Coulomb repulsion between opposite spins [38, 39]. Note that different values have been considered for parameter U in the other studies on zigzag edges, which indicate the obtained results based on mean-field Hubbard approximation can be slightly varied (quantitatively) when U is varied [40, 41]. The average value of spin occupation operator $\langle n_{i\sigma}\rangle$ is given as

$$\langle n_{i\sigma}\rangle = \sum_{\text{bands}} \frac{a}{2\pi}\int_0^{2\pi/a} g_{i\sigma}(k)\mathrm{d}k, \tag{4}$$

the parameter a denotes the width of the unit cell of ZGNR electrodes and $g_{i\sigma}(k)$ is the spin-dependent electron density at the site i. $\langle n_{i\sigma}\rangle$ can be solved self-consistently by an iteration method from equations (3) and (4) [42].

The transport in two spin channel is assumed independently, spin-flip processes can be neglected due to long spin-diffusion length in graphene nanostructures [43] and C_{60} [7, 8]. The spin-resolved transmission function through the scattering region is obtained by [44, 45]

$$\mathrm{T}_\sigma(\varepsilon) = \mathrm{Tr}\left[\Gamma_{\mathrm{L},\sigma}(\varepsilon)G_{\mathrm{C},\sigma}(\varepsilon)\Gamma_{\mathrm{R},\sigma}(\varepsilon)G^{\dagger}_{\mathrm{C},\sigma}(\varepsilon)\right], \tag{5}$$

where, $G_{\mathrm{C},\sigma} = \left[(\varepsilon + i0^+)I - \mathcal{H}_{\mathrm{C}} - \sum_{\mathrm{L},\sigma} - \sum_{\mathrm{R},\sigma}\right]^{-1}$ is the Green's function of the device, in which $\sum_{\mathrm{L(R)},\sigma} = \mathcal{V}_{\mathrm{CL(CR)}}\mathrm{g}_{\mathrm{L(R)},\sigma}(\varepsilon)\mathcal{V}^{\dagger}_{\mathrm{CL(CR)}}$ is the left (right) self-energy. $\mathrm{g}_{\mathrm{L(R)},\sigma} = \left[(\varepsilon + i0^+)I - \mathcal{H}^{00}_{\mathrm{L(R)},\sigma} - \mathcal{H}^{01}_{\mathrm{L(R)}}T_{\mathrm{L(R)},\sigma}\right]^{-1}$ is the surface Green's function of the left (right) electrode, which is considered spin-dependent due to magnetic structure of the electrodes. In the latter equation, $\mathcal{H}^{01}_{\mathrm{L(R)}}$ is the hopping matrix between two adjacent unit cells at the left (right) electrode, and $T_{\mathrm{L(R)},\sigma}$ is the transfer matrix of the left (right) electrode and can be determined by iteration method [46]. Finally in equation (5), $\Gamma_{\mathrm{L(R)},\sigma}(\varepsilon) = -2\,\mathrm{Im}\left[\sum_{\mathrm{L(R)},\sigma}(\varepsilon)\right]$ describes the coupling scattering region with the left (right) electrode. For more clarity, a matrix form for the Hamiltonian of the 6-ZGNR electrodes and the scattering region is presented in appendix A.

The thermal gradient along the device creates a difference in the spin carriers distribution around the Fermi level of electrodes, which leads to inducing thermal spin current across the device. Spin-resolved current across the device in the Landauer–Büttiker formalism is obtained as [44, 47]

$$I_\sigma = \frac{e}{h}\int_{-\infty}^{+\infty} \mathrm{T}_\sigma(\varepsilon)\,[f_{\mathrm{L}}(\varepsilon, T_{\mathrm{L}}) - f_{\mathrm{R}}(\varepsilon, T_{\mathrm{R}})]\,\mathrm{d}\varepsilon, \tag{6}$$

where $f_{\mathrm{L(R)}}$, is the Fermi–Dirac distribution of the left (right) electrode. e, h, and $T_{\mathrm{L(R)}}$ are the electron charge, the Planck constant, and the left (right) electrode temperature, respectively. Moreover, the spin TP in the linear response regime is given as [48]

$$\mathrm{TP_s} = -\frac{\Delta V_{\mathrm{s}}}{\Delta T} = (\mathrm{TP}_\alpha - \mathrm{TP}_\beta), \tag{7}$$

where ΔV_{s} and $\Delta T = T_{\mathrm{L}} - T_{\mathrm{R}}$ is defined as the spin-voltage difference induced by temperature gradient and the temperature difference of electrodes, respectively. Also, $\mathrm{TP}_\sigma = -(1/|e|T)(L_{1\sigma}/L_{0\sigma})$ is the spin-resolved thermopower, where $L_{n\sigma}(\mu, T) = (-1/h)\int\{\partial f(\varepsilon, \mu, T)/\partial\varepsilon\}(\varepsilon - \mu)^n T_\sigma(\varepsilon)\mathrm{d}\varepsilon (n = 0, 1)$ [45, 47]. Note that numerical results show that the linear and nonlinear transport theories have a very high agreement under condition $|\Delta T| \lesssim (T_{\mathrm{L}} + T_{\mathrm{R}})/2$ [49]. Moreover, we define the thermally-induced MR as $\mathrm{MR_T} = (|I_{\mathrm{FM}}| - |I_{\mathrm{AFM}}|)/(|I_{\mathrm{FM}}| + |I_{\mathrm{AFM}}|) \times 100$ when switching from FM to AFM configuration and conversely, where I_{FM} (I_{AFM}) is the induced charge current, $I_{\mathrm{ch}} = I_\alpha + I_\beta$, for FM (AFM) configuration under temperature gradient.

3. Results and discussion

Figures 2(a) and (b) shows the spin-resolved transmission function as red (α-spin, T_α) and blue (β-spin, T_β) filled areas for AFM and FM configurations, respectively. As expected, the transmission for AFM configuration is completely similar in both spin channels, as shown in figure 2(a). Interestingly, the β-spin transmission for FM configuration around the Fermi level is nearly zero, which indicates the β-spin channel is blocked for transport, in spite of the conductive α-spin channel. The spin polarization of transmission $P = (T_\alpha - T_\beta)/(T_\alpha + T_\beta) \times 100$ at the Fermi level is close to 100% and thus, FM configuration exhibits the half-metallic nature at the Fermi level. Moreover, Far from the Fermi level, the spin-polarized and narrow transmission peaks are observed. Furthermore, the spin-resolved current spectra, $J_\sigma(\varepsilon) = (f_{\mathrm{L}} - f_{\mathrm{R}})T_\sigma(\varepsilon)$, is plotted for AFM and FM configurations as a function of energy at $T_{\mathrm{L}} = 300$ K for $\Delta T =$ 20 and 50 K. As can be seen, the contribution of electrons dominates the contribution of holes in both configurations around the Fermi level, which leads to generating the negative currents. In FM configuration, the current spectra in the β-spin channel are much smaller compared to the α-spin channel. These behaviors can produce different spin currents in AFM and FM configurations as a function of the temperature gradient.

Thermally-generated spin currents I_σ as a function of T_{L} and ΔT at $\mu = 0$ is presented in figure 3 for AFM and FM configurations of ZZ-C60D-ZZ. Applying temperature gradient in AFM configuration is generated equal currents in α- and β-spin channels (I_α and I_β), which is clearly seen in figures 3(a) and (b). The similar currents were expected due to the similar transmission in both spin channels of AFM configuration. While, current in α- and β-spin channels is quite different for FM configuration, as can be seen in figures 3(c) and (d). The current in β-spin channel of FM configuration is nearly zero even with increasing T_{L} and ΔT, while the α-spin current increases by increasing T_{L} and ΔT. These results demonstrate the existence of a spin-filtering behavior at the FM configuration of ZZ-C60D-ZZ, which has a perfect match with the transmission coefficient of the α-spin channel (see figure 2(b)). Moreover, the current in AFM configuration is almost one order smaller than the current in α-spin channel of FM configuration because of the difference of their current

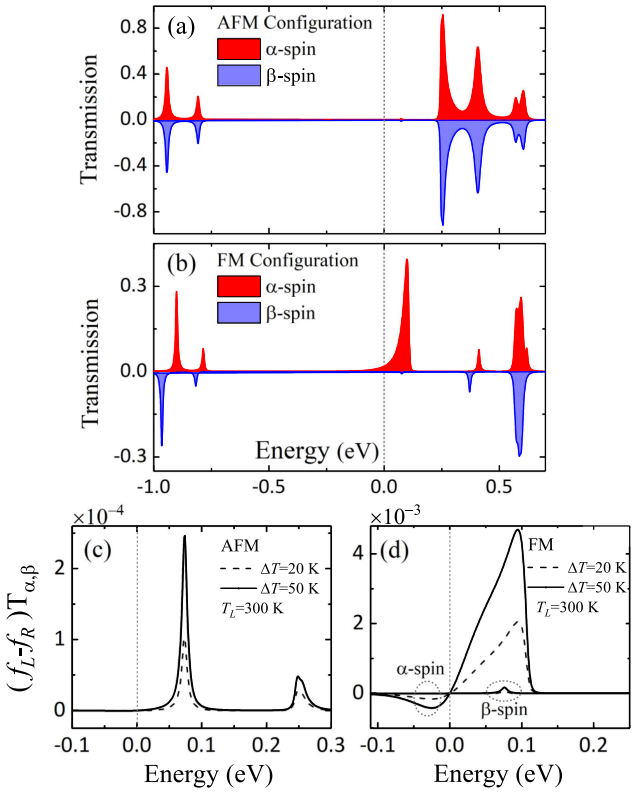

Figure 2. (a) and (b) show the transmission coefficient of α- and β-spin channels in AFM and FM configurations, respectively. (c) and (d) show the spin-resolved current spectra at $T_{\rm L} = 300$ K for $\Delta T = 20$ and 50 K.

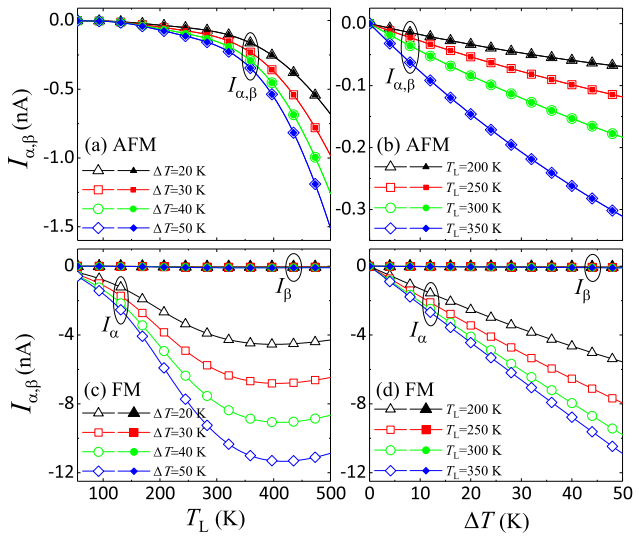

Figure 3. Flowing currents from α- and β-spin channels as a function of $T_{\rm L}$ and ΔT. Open and solid symbol present I_α and I_β, respectively. Panels (a) and (b) for the AFM configuration, and (c) and (d) for the FM configuration.

spectra, which is quite clear in figures 2(c) and (d). The negative sign of currents is due to the predominance of electrons to holes, as in figures 2(c) and (d) is observed that current spectra above the Fermi level are superior to that below.

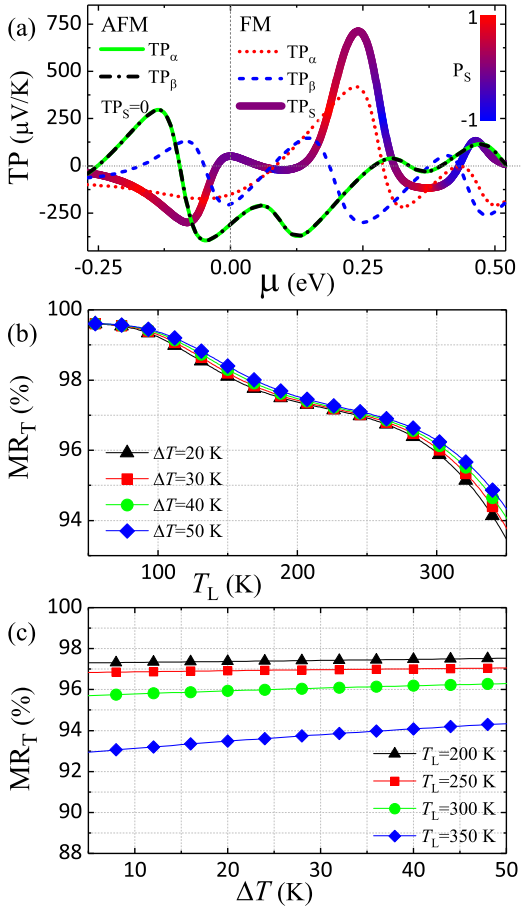

Figure 4. (a) α-spin and β-spin thermopower (TP_α and TP_β) for AFM and FM configurations, and spin thermopower ($\mathrm{TP_s}$, wide colored line) for FM configuration as a function of chemical potential at $T = 300$ K. (b) and (c) thermally-induced MR as a function of $T_{\rm L}$ and ΔT, respectively.

Spin-resolved and spin TP coefficients (TP_α, TP_β, and $\mathrm{TP_S}$) as a function of chemical potential at $T = 300$ K are presented in figure 4(a), for both AFM and FM cases. As can be seen, TP_α and TP_β for the AFM configuration are completely the same due to the symmetry of α- and β-spin transmission which lead to zero $\mathrm{TP_S}$. While, TP in α- and β-spin channels for FM configuration has different values which are shown with red dotted and blue dashed lines, respectively. Therefore, $\mathrm{TP_S}$ for FM configuration is nonzero, shown as wide colored line in figure 4(a). Maximum value of $\mathrm{TP_S}$ for FM configuration is located at $\mu \simeq 0.24$ eV and equal to 710 μV/K. At this chemical potential, TP_α and TP_β are at their maximum with the opposite sign, which leads to significant $\mathrm{TP_S}$, unlike other chemical potentials. The obtained $\mathrm{TP_s}$ value is comparable to reported values for graphene nanoribbon devices [34, 47, 50] and all-carbon molecular junctions [51–53]. Furthermore, this is higher than the maximum measured value of charge TP (460 μV/K) for graphene-fullerene TE nanodevice [29]. The color of $\mathrm{TP_S}$ curve indicates its polarization, $P_{\rm s} = (|\mathrm{TP}_\alpha| - |\mathrm{TP}_\beta|)/(|\mathrm{TP}_\alpha| + |\mathrm{TP}_\beta|)$, which represents the effect of each spin channel on $\mathrm{TP_s}$.

Finally, we investigate the thermally-induced MR ($\mathrm{MR_T}$) because of changing the magnetization of the electrodes; from

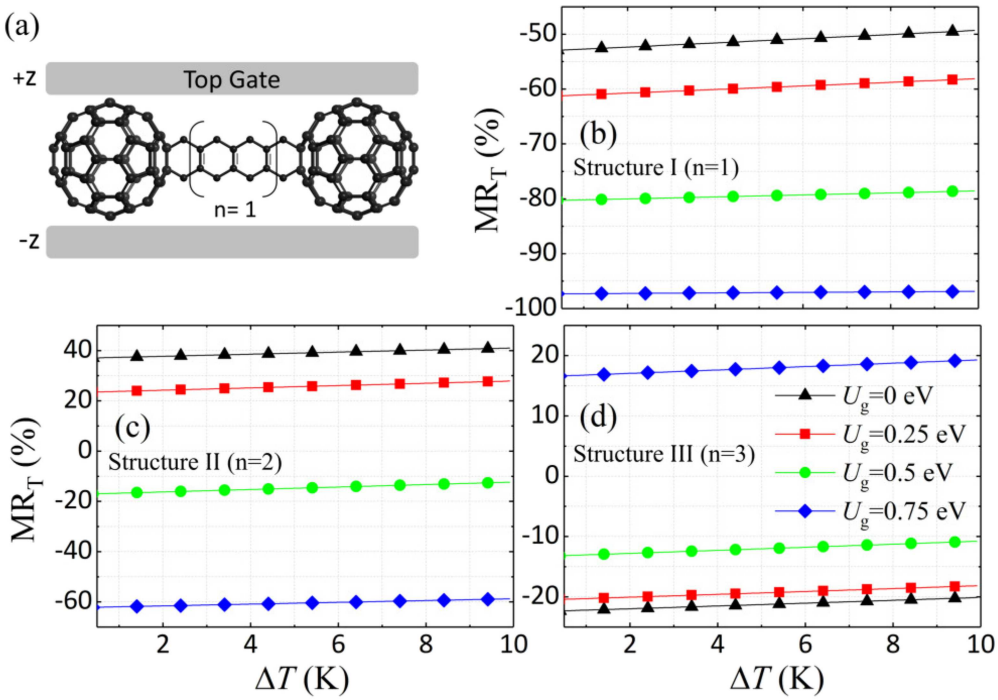

Figure 5. (a) Dumbbell-like system in which a pair of C_{60} units are linked through cyclohexa-1,4-dienyl ladder with $n = 1$. (b)–(d) Thermal MR of structures I($n = 1$), II($n = 2$), and III($n = 3$), respectively, as a function of ΔT for different gate voltages.

FM to the AFM state. Thermal MR are plotted as a function of T_L and ΔT in figures 4(b) and (c), respectively. As shown in figure 4(b), MR_T is close to 100% in low temperatures of T_L and up to about 100 K. This can happen when there is no current in one magnetic configuration or is negligible compared to the other configuration. In low temperatures, charge current (the sum of α- and β-spin currents) for AFM configuration (I_{AFM}) is almost zero and for FM configuration (I_{FM}) is nonzero (see figure 3), as a result, according to the MR relation, MR_T is about 100%. However, I_{AFM} gradually increases in higher temperatures, which lead to reduction of MR_T and reaches to approximate value of 96% at 300 K. As seen in figure 4(c), MR_T gradually decreases by increasing T_L from 200–350 K. However, MR_T has a significant value even at room temperature. Furthermore, as can be seen in figure 4(c), MR_T does not change significantly with respect to temperature difference changes, so that increasing ΔT slightly increases MR_T, which is due to the negligible current in the AFM compared to FM configuration at different temperatures. The MR values obtained in this study are significantly higher than those reported in other studies, especially the experimental results. Primarily, this discrepancy stems from the limitation of applying all the conditions of an experimental study to theoretical computation. Also, different expressions have been proposed for MR in the literature that can cause a discrepancy in reported MR.

To investigate the ability to induce giant MR in C_{60} dimer, we considere the other C_{60} dimers. The two C_{60} molecules are linked through cyclohexa-1,4-dienyl ladders with three different length, $n = 1$, 2 and 3 [54, 55]. We specify these structures with symbols I($n = 1$), II($n = 2$), and III($n = 3$). Figure 5(a) shows C_{60} dimer with $n = 1$. These structures can be stable much above the room temperature [54]. Like the structures shown in figures 1(a) and (b), these C_{60} dimers were considered as the scattering region between two semi-infinite 6-ZGNRs for two FM and AFM configurations. These structures reveal the thermal MR in the absence of the voltage bias; however, for optimizing the MR, we study the effect of different external gate voltages on the thermal MR. The gate voltage covers all atoms in the scattering region, which can be applied through the two gate stripes in the z-direction. The gate voltage induces the potential energy U_g on the on-site term in the Hamiltonian of the scattering region. Note that U_g value in each site is proportional to its z-axis coordinate. Therefore, the potential energy varies in the closed interval of $[-U_g, U_g]$ eV, where the values of the beginning and end of the interval related to the atoms with coordinates $-z$ and z, respectively. Thermal MR of structures I, II, and III as a function of ΔT for different U_g are presented in figures 5(b)–(d). Interestingly, the thermally-induced MR in all C_{60} junctions are strongly dependent on the values of U_g. As can be seen, the absolute value of thermal MR gradually decreases by increasing the length of ladder for different U_g. Structure I at $U_g = 0$ is negative and gradually increases with increasing U_g, therefore reaches nearly 100% at $U_g = 0.75$ eV but remains negative (see figure 5(b)). Structure II at $U_g = 0$ has positive thermal MR and as U_g increases, first decreases at the positive values and then increases until $\sim 60\%$ at the negative values (see figure 5(c)). Thermal MR of structure III is first reduced and then increased as U_g rises (see figure 5(d)). Furthermore, thermal MR increases with slight slope as ΔT increases for all of the structures.

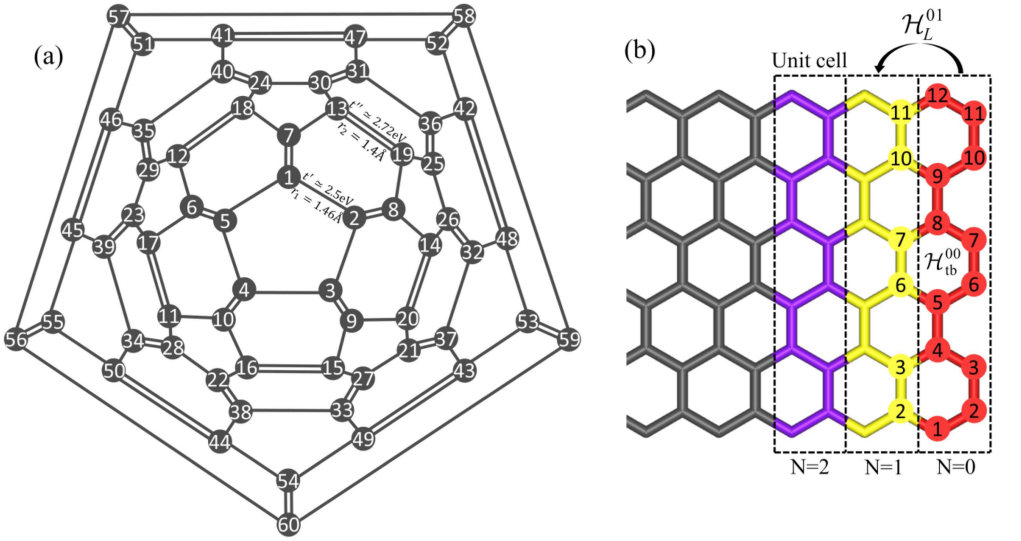

Figure A.1. (a) Schematic view of the C_{60} molecule with presenting single and double bonds, and (b) zigzag-edge graphene nanoribbon with index 6.

It should be noted that the design of atomic configuration, especially in low dimensional materials, has always been one of the most important challenges to achieving high TE efficiency. Some of these designs are aimed at engineering the energy band structure [56, 57] to increase the Seebeck coefficient, and some of them are designed to decrease thermal conductivity, which ultimately improves TE efficiency. In this regard, defect and bandgap engineering are strategies to reduce the lattice thermal conductivity and enhance the Seebeck coefficient without dramatically degrading the electronic conductance in carbon nanostructures. Beside all designed configurations, ours is also an excellent choice to optimize the thermopower. Moreover, the mismatch in phonon modes of the semi-infinite ZGNR electrode and the C_{60} dimers can reduce the phonon thermal conductivity across the junction. Furthermore, despite the simple structure of the electrodes, we get amazing results compared to our earlier study. In detail, in our previous study [35, 47], we investigated the spin-related TE properties based on periodic structures of carbon nanostructures, which magnetism is present throughout the system. While structures in the present study and recently published work [58] have been designed as a non-periodic molecular junction which, in the later one, we could generate a spin-dependent current. While here, based on C_{60} junction and intrinsic edge magnetism in ZGNR, a giant MR in addition to the spin current can be obtained. Moreover, contrary to our previous study, half-metallic nature appeared for FM configuration in the C_{60} junction, which leads to the existence of current in one of the spin channels and could have a large application in spin-related TE devices.

4. Conclusion

In summary, applying the equilibrium Green's function method and Landauer–Büttiker transport formalism, we theoretically investigated the spin-related thermoelectric (TE) effects in a molecular junction. This device consists of C_{60} dimer and zigzag graphene nanoribbon (ZGNR) as electrodes. The electronic and transport properties of our proposed molecular junction are susceptible to the magnetic configuration of ZGNR electrodes. Therefore, anti-ferromagnetic (AFM) and ferromagnetic (FM) configurations reveal the semi-conductive and half-metallic phases, respectively. Moreover, these properties induce the different currents by an applied thermal gradient in both FM and AFM configurations, which lead to zero and nonzero spin thermopower in AFM and FM configurations, respectively. The proposed device indicates a giant thermal MR behavior when switching between AFM and FM configurations, which can preserve even at room temperature. Furthermore, the thermal MR remarkably improves under an external gate voltage for the other C_{60} dimers with different lengths of cyclohexa-1, 4-dienyl ladders. Finally, obtained results are comparable to molecular junction devices, which show our proposed device can be deserved to be brought into the attention, experimentally.

Appendix A. Hamiltonian matrix form

In this appendix, we present a matrix form for Hamiltonian of the ZGNR electrodes and scattering region in the real space. The Hamiltonian of scattering region is a 120×120 matrix, with respect to 120 atomic sites of C_{60} dimer. Here, we present the Hamiltonian matrix for the C_{60} molecule, the C_{60} dimers being calculated similarly. A schematic view of the C_{60} molecule based on the symmetry group [59] is presented in figure A.1(a). In this diagram, using the hopping energy of single and double bonds (t', t'') and the number of each carbon atom in the C_{60} molecule, the Hamiltonian matrix in TB model can easily be constructed as a 60×60 matrix

$$\mathcal{H}_{C_{60}} = \begin{pmatrix} 0 & t'_{1,2} & 0 & 0 & t'_{1,5} & 0 & t''_{1,7} & 0 & 0 & 0 & 0 & \dots \\ t'_{2,1} & 0 & t'_{2,3} & 0 & 0 & 0 & 0 & t''_{2,8} & 0 & 0 & 0 & \dots \\ 0 & t'_{3,2} & 0 & t'_{3,4} & 0 & 0 & 0 & 0 & t''_{3,9} & 0 & 0 & \dots \\ 0 & 0 & t'_{4,3} & 0 & t'_{4,5} & 0 & 0 & 0 & 0 & t''_{4,10} & 0 & \dots \\ t'_{5,1} & 0 & 0 & t'_{5,4} & 0 & t''_{5,6} & 0 & 0 & 0 & 0 & 0 & \dots \\ \vdots & \vdots & \vdots & \vdots & \vdots & \vdots & \vdots & \vdots & \vdots & \vdots & \vdots & \ddots \end{pmatrix}_{60\times 60}, \tag{A.1}$$

each carbon atom in the C_{60} molecule is connected to three atoms. Therefore, there are three non-zero elements in each row or column of the matrix, which denoted by t' and t''. Note that only the matrix elements are corresponding to the central pentagonal ring of figure A.1(a) are specified. Now, we present a matrix form for Hamiltonian of the 6-ZGNR electrodes. Consider figure A.1(b), which shows the 6-ZGNR contains twelve atomic sites per unit cell. The spin-dependent Hamiltonian for a unit cell is given by equation (3), in which, $\mathcal{H}_{tb}^{00}$ is provided by the following matrix concerning figure A.1(b).

$$\mathcal{H}_{tb}^{00} = \begin{pmatrix} 0 & t_{1,2} & 0 & 0 & 0 & 0 & 0 & \dots \\ t_{2,1} & 0 & t_{2,3} & 0 & 0 & 0 & 0 & \dots \\ 0 & t_{3,2} & 0 & t_{3,4} & 0 & 0 & 0 & \dots \\ 0 & 0 & t_{4,3} & 0 & t_{4,5} & 0 & 0 & \dots \\ 0 & 0 & 0 & t_{5,4} & 0 & t_{5,6} & 0 & \dots \\ \vdots & \vdots & \vdots & \vdots & \vdots & \vdots & \vdots & \ddots \end{pmatrix}_{12\times 12}, \tag{A.2}$$

in this matrix, $t_{i,j} \simeq 2.6\,\text{eV}$ is considered. Moreover, $\mathcal{H}_{U,\alpha}$ in equation (3) is written in the following matrix form

$$\mathcal{H}_{U,\alpha} = U \begin{pmatrix} \langle n_{1\beta}\rangle[n_{1\alpha} - (1/2)\langle n_{1\alpha}\rangle] & 0 & 0 & \dots \\ 0 & \langle n_{2\beta}\rangle[n_{2\alpha} - (1/2)\langle n_{2\alpha}\rangle] & 0 & \dots \\ 0 & 0 & \langle n_{3\beta}\rangle[n_{3\alpha} - (1/2)\langle n_{3\alpha}\rangle] & \dots \\ \vdots & \vdots & \vdots & \ddots \end{pmatrix}_{12\times 12}, \tag{A.3}$$

and $\mathcal{H}_{U,\beta}$ is similarly formed. In addition, $\mathcal{H}_{L(R)}^{01}$ in the surface Green's function is given by the following matrix with respect to the two adjacent unit cells in figure A.1(b)

$$\mathcal{H}_{L}^{01} = (\mathcal{H}_{R}^{01})^{\dagger} = \begin{pmatrix} 0 & t_{1,2} & 0 & 0 & 0 & 0 & 0 & \dots \\ 0 & 0 & 0 & 0 & 0 & 0 & 0 & \dots \\ 0 & 0 & 0 & 0 & 0 & 0 & 0 & \dots \\ 0 & 0 & t_{4,3} & 0 & 0 & 0 & 0 & \dots \\ 0 & 0 & 0 & 0 & 0 & t_{5,6} & 0 & \dots \\ \vdots & \vdots & \vdots & \vdots & \vdots & \vdots & \vdots & \ddots \end{pmatrix}_{12\times 12}, \tag{A.4}$$

here, $t_{i,j} \simeq 2.6\,\text{eV}$ is considered.

ORCID iDs

Rouhollah Farghadan https://orcid.org/0000-0001-6499-3230

References

[1] Pang R, Shi X and Van Hove M A 2016 *J. Am. Chem. Soc.* **138** 4029–35
[2] Bobbert P A 2014 *Science* **345** 1450–1
[3] Rocha A R, Garcia-Suarez V M, Bailey S W, Lambert C J, Ferrer J and Sanvito S 2005 *Nat. Mater.* **4** 335
[4] Sanvito S 2007 *Nat. Nanotechnol.* **2** 204
[5] Dediu V A, Hueso L E, Bergenti I and Taliani C 2009 *Nat. Mater.* **8** 707
[6] Sanvito S 2011 *Chem. Soc. Rev.* **40** 3336–55
[7] Yu Z 2012 *Phys. Rev.* B **85** 115201
[8] Zhang X, Mizukami S, Kubota T, Ma Q, Oogane M, Naganuma H, Ando Y and Miyazaki T 2013 *Nat. Commun.* **4** 1392
[9] Liu H, Wang J, Groesbeck M, Pan X, Zhang C and Vardeny Z V 2018 *J. Mater. Chem.* C **6** 3621–7
[10] Zhang X, Ai X, Zhang R, Ma Q, Wang Z, Qin G, Wang J, Wang S, Suzuki K, Miyazaki T *et al* 2016 *Carbon* **106** 202–7
[11] Tran T L A, Le T Q, Sanderink J G, van der Wiel W G and de Jong M P 2012 *Adv. Funct. Mater.* **22** 1180–9
[12] Li F, Li T, Chen F and Zhang F 2014 *Org. Electron.* **15** 1657–63
[13] Gobbi M, Golmar F, Llopis R, Casanova F and Hueso L E 2011 *Adv. Mater.* **23** 1609–13
[14] Moorsom T, Wheeler M, Khan T M, Al Ma'Mari F, Kinane C, Langridge S, Bedoya-Pinto A, Hueso L, Teobaldi G, Lazarov V K *et al* 2014 *Phys. Rev.* B **90** 125311
[15] Cakır D, Otálvaro D M and Brocks G 2014 *Phys. Rev.* B **90** 245404
[16] Saffarzadeh A and Kirczenow G 2013 *Appl. Phys. Lett.* **102** 173101
[17] Sanvito S 2010 *Nat. Phys.* **6** 562
[18] Barraud C, Seneor P, Mattana R, Fusil S, Bouzehouane K, Deranlot C, Graziosi P, Hueso L, Bergenti I, Dediu V *et al* 2010 *Nat. Phys.* **6** 615

[19] Sadeghi H, Sangtarash S and Lambert C 2017 *Nano Lett.* **17** 4611–8
[20] Ullmann K, Coto P B, Leitherer S, Molina-Ontoria A, Martín N, Thoss M and Weber H B 2015 *Nano Lett.* **15** 3512–8
[21] Lau C S, Sadeghi H, Rogers G, Sangtarash S, Dallas P, Porfyrakis K, Warner J, Lambert C J, Briggs G A D and Mol J A 2016 *Nano Lett.* **16** 170–6
[22] Kim Y, Jeong W, Kim K, Lee W and Reddy P 2014 *Nat. Nanotechnol.* **9** 881
[23] Rincón-García L, Ismael A K, Evangeli C, Grace I, Rubio-Bollinger G, Porfyrakis K and Lambert C J 2016 *Nat. Mater.* **15** 289
[24] Evangeli C, Gillemot K, Leary E, Gonzalez M T, Rubio-Bollinger G, Lambert C J and Agraït N 2013 *Nano Lett.* **13** 2141–5
[25] Lee S K, Ohto T, Yamada R and Tada H 2014 *Nano Lett.* **14** 5276–80
[26] Klöckner J C, Siebler R, Cuevas J C and Pauly F 2017 *Phys. Rev.* B **95** 245404
[27] Yee S K, Malen J A, Majumdar A and Segalman R A 2011 *Nano Lett.* **11** 4089–94
[28] Wu Q, Sadeghi H, García-Suárez V M, Ferrer J and Lambert C J 2017 *Sci. Rep.* **7** 11680
[29] Gehring P, Harzheim A, Spiece J, Sheng Y, Rogers G, Evangeli C, Mishra A, Robinson B J, Porfyrakis K, Warner J H *et al* 2017 *Nano Lett.* **17** 7055–61
[30] Khalatbari H, Vishkayi S I and Soleimani H R 2019 *Physica* E **108** 372–81
[31] Zhou P, Dong Z H, Rao A and Eklund P 1993 *Chem. Phys. Lett.* **211** 337–40
[32] Son Y W, Cohen M L and Louie S G 2006 *Nature* **444** 347
[33] Magda G Z, Jin X, Hagymási I, Vancsó P, Osváth Z, Nemes-Incze P, Hwang C, Biró L P and Tapasztó L 2014 *Nature* **514** 608
[34] Shirdel-Havar M and Farghadan R 2018 *Phys. Rev.* B **97** 235421
[35] Shirdel-Havar M and Farghadan R 2019 *J. Phys. Chem.* C **123** 20105–15
[36] Manousakis E 1991 *Phys. Rev.* B **44** 10991
[37] Chen X, Liu Y, Gu B L, Duan W and Liu F 2014 *Phys. Rev.* B **90** 121403
[38] Zamani S and Farghadan R 2019 *Phys. Rev.* B **99** 235418
[39] Liu W, Wang Z F, Shi Q W, Yang J and Liu F 2009 *Phys. Rev.* B **80** 233405
[40] Yazyev O V 2008 *Phys. Rev. Lett.* **101** 037203
[41] Fernández-Rossier J and Palacios J J 2007 *Phys. Rev. Lett.* **99** 177204
[42] Zamani S and Farghadan R 2018 *Phys. Rev. Appl.* **10** 034059
[43] Tombros N, Tanabe S, Veligura A, Jozsa C, Popinciuc M, Jonkman H and Van Wees B 2008 *Phys. Rev. Lett.* **101** 046601
[44] Tan X Y, Wu D D, Liu Q B, Fu H H and Wu R 2018 *J. Phys.: Condens. Matter* **30** 355303
[45] Zhou B, Zhou B, Chen X, Liao W and Zhou G 2015 *J. Phys.: Condens. Matter* **27** 465301
[46] Nardelli M B 1999 *Phys. Rev.* B **60** 7828
[47] Shirdel-Havar M and Farghadan R 2018 *Phys. Chem. Chem. Phys.* **20** 16853
[48] Rejec T, Mravlje J, Ramšak A *et al* 2012 *Phys. Rev.* B **85** 085117
[49] Azema J, Lombardo P and Daré A M 2014 *Phys. Rev.* B **90** 205437
[50] Zhou B, Zhou B, Yao Y, Zhou G and Hu M 2017 *J. Phys.: Condens. Matter* **29** 405303
[51] Li J, Wang B, Xu F, Wei Y and Wang J 2016 *Phys. Rev.* B **93** 195426
[52] Liu Y, Shao X, Shao T, Zhang J, Kuang Y, Zhang D, Shao Z, Yu H, Hong X, Feng J *et al* 2016 *Carbon* **109** 411–7
[53] Liu Y S, Zhang X, Feng J F and Wang X F 2014 *Appl. Phys. Lett.* **104** 242412
[54] Paquette L A and Graham R J 1995 *J. Org. Chem.* **60** 2958–9
[55] Segura J L and Martín N 2000 *Chem. Soc. Rev.* **29** 13–25
[56] Pei Y, Wang H and Snyder G J 2012 *Adv. Mater.* **24** 6125–35
[57] Zeier W G, Zevalkink A, Gibbs Z M, Hautier G, Kanatzidis M G and Snyder G J 2016 *Angew. Chem., Int. Ed.* **55** 6826–41
[58] Ildarabadi F and Farghadan R 2020 *J. Magn. Magn. Mater.* **497** 165980
[59] Ellzey M L Jr 2007 *J. Comput. Chem.* **28** 811–7